NASA/TM-1999-209526

Unstructured Grid Euler Method Assessment for Longitudinal and Lateral/ Directional Stability Analysis of the HSR Reference H Configuration at Transonic Speeds

Farhad Ghaffari
Langley Research Center, Hampton, Virginia

December 1999

The NASA STI Program Office . . . in Profile

Since its founding, NASA has been dedicated to the advancement of aeronautics and space science. The NASA Scientific and Technical Information (STI) Program Office plays a key part in helping NASA maintain this important role.

The NASA STI Program Office is operated by Langley Research Center, the lead center for NASA's scientific and technical information. The NASA STI Program Office provides access to the NASA STI Database, the largest collection of aeronautical and space science STI in the world. The Program Office is also NASA's institutional mechanism for disseminating the results of its research and development activities. These results are published by NASA in the NASA STI Report Series, which includes the following report types:

- TECHNICAL PUBLICATION. Reports of completed research or a major significant phase of research that present the results of NASA programs and include extensive data or theoretical analysis. Includes compilations of significant scientific and technical data and information deemed to be of continuing reference value. NASA counterpart of peer-reviewed formal professional papers, but having less stringent limitations on manuscript length and extent of graphic presentations.

- TECHNICAL MEMORANDUM. Scientific and technical findings that are preliminary or of specialized interest, e.g., quick release reports, working papers, and bibliographies that contain minimal annotation. Does not contain extensive analysis.

- CONTRACTOR REPORT. Scientific and technical findings by NASA-sponsored contractors and grantees.

- CONFERENCE PUBLICATION. Collected papers from scientific and technical conferences, symposia, seminars, or other meetings sponsored or co-sponsored by NASA.

- SPECIAL PUBLICATION. Scientific, technical, or historical information from NASA programs, projects, and missions, often concerned with subjects having substantial public interest.

- TECHNICAL TRANSLATION. English-language translations of foreign scientific and technical material pertinent to NASA's mission.

Specialized services that complement the STI Program Office's diverse offerings include creating custom thesauri, building customized databases, organizing and publishing research results . . . even providing videos.

For more information about the NASA STI Program Office, see the following:

- Access the NASA STI Program Home Page at ***http://www.sti.nasa.gov***

- Email your question via the Internet to help@sti.nasa.gov

- Fax your question to the NASA STI Help Desk at (301) 621-0134

- Telephone the NASA STI Help Desk at (301) 621-0390

- Write to:
  NASA STI Help Desk
  NASA Center for AeroSpace Information
  7121 Standard Drive
  Hanover, MD 21076-1320

NASA/TM-1999-209526

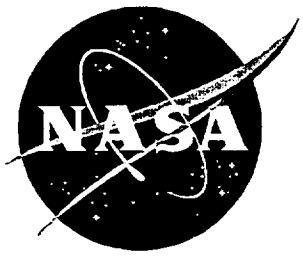

Unstructured Grid Euler Method Assessment for Longitudinal and Lateral/ Directional Stability Analysis of the HSR Reference H Configuration at Transonic Speeds

Farhad Ghaffari
Langley Research Center, Hampton, Virginia

National Aeronautics and
Space Administration

Langley Research Center
Hampton, Virginia 23681-2199

December 1999

Available from:

NASA Center for AeroSpace Information (CASI)
7121 Standard Drive
Hanover, MD 21076-1320
(301) 621-0390

National Technical Information Service (NTIS)
5285 Port Royal Road
Springfield, VA 22161-2171
(703) 605-6000

Unstructured Grid Euler Method Assessment for Longitudinal and Lateral/Directional Stability Analysis of the HSR Reference H Configuration at Transonic Speeds

Farhad Ghaffari
NASA Langley Research Center, Hampton, VA

ABSTRACT

Transonic Euler computations, based on unstructured grid methodology, are performed for a proposed High Speed Civil Transport (HSCT) configuration, designated as the Reference H configuration within the High Speed Research (HSR) Program. The predicted results are correlated with appropriate experimental wind-tunnel data for the baseline configuration with and without control surface deflections for a range of angle of attack at $M_\infty = 0.95$. Good correlations between the predictions and measured data have been obtained for the longitudinal aerodynamic characteristics on the baseline configuration. The incremental effects in the longitudinal aerodynamic characteristics due to horizontal tail deflections as well as wing leading-edge and trailing-edge flap deflections have also been predicted reasonably well. Computational results and correlations with data are also presented for the lateral and directional stability characteristics for a range of angle of attack at a constant sideslip angle as well as a range of sideslip angles at a constant angle of attack. In addition, the results are presented to assess the computational method performance and convergence characteristics.

SYMBOLS

b_{ref}	reference span, inches
$\bar{c}$	reference chord, inches
C_D	drag coefficient, Drag/$(q_\infty\ S_{ref})$
C_{Do}	skin friction drag at $C_L = 0$
C_L	lift coefficient, Lift/$(q_\infty\ S_{ref})$
C_l	rolling moment coefficient, Rolling moment/$(q_\infty\ S_{ref}\ b_{ref})$
C_m	pitching moment coefficient, Pitching moment/$(q_\infty\ S_{ref}\ \bar{c})$
C_n	Yawing moment coefficient, Yawing moment/$(q_\infty\ S_{ref}\ b_{ref})$
C_p	pressure coefficient, $(p - p_\infty)/q_\infty$
M_∞	freestream Mach number
p	static pressure
p_∞	freestream static pressure
q_∞	freestream dynamic pressure
R_{ft}	Reynolds number per foot
S_{ref}	reference area, sq. inches
α	angle of attack, degrees
β	sideslip angle, degrees
δ_{ht}	horizontal tail flap deflection angle, degrees
δ_{lef}	inboard/outboard wing leading-edge flap deflection angle, degrees
δ_{tef}	inboard/outboard wing trailing-edge flap deflection angle, degrees

Abbreviations

HSCT	High Speed Civil Transport
HSR	High Speed Research
IGES	Initial Graphics Exchange Specification
LaRC	Langley Research Center

COMPUTATIONAL OBJECTIVE AND APPROACH

The primary objective of the computations is to provide an accuracy assessment of an unstructured grid Euler method known as USM3D (Ref. 1) for predicting the longitudinal and lateral/directional aerodynamic characteristics for the baseline configuration and the corresponding effects due to control surface deflections at transonic speeds.

A computational matrix is developed to complement the configurations and the conditions tested in the NASA LaRC 16-Foot Transonic Tunnel. The wind tunnel test was conducted on a 1.675% model (also referred to as controls model) at an average Reynolds number of about 4 million per foot. Three configurations are selected for the computational method assessment study. Consistent with the experimental test, each configuration incorporated an extended circular aftbody to represent the wind-tunnel model sting apparatus and appropriate boundary conditions at the nacelle's inlet and exhaust planes to simulate the flow through propulsion effects. The selected configurations are:

1) transonic cruise (i.e., $\delta_{lef} = 0/10$; $\delta_{tef} = 0/3$; $\delta_{ht} = 0$). This geometry is considered as the baseline transonic cruise configuration.

2) transonic cruise with deflected horizontal tail (i.e., $\delta_{lef} = 0/10$; $\delta_{tef} = 0/3$; $\delta_{ht} = 6$).

3) supersonic cruise configuration where all the control surface deflection angles are set to zero (i.e., $\delta_{lef} = 0/0$; $\delta_{tef} = 0/0$; $\delta_{ht} = 0$).

The above nomenclatures are defined as: the Greek letter δ represents control surface deflection angle; the subscripts lef, tef, and ht denote the leading-edge flap, trailing-edge flap, and horizontal tail, respectively. If applicable, the control surface deflection angles, separated by a slash, correspond to those of the inboard and outboard wing, respectively. For example, $\delta_{lef} = 0/10$ denotes that the inboard- and outboard-wing segmented leading-edge flap deflection angles are set to 0° and 10°, respectively. The positive control surface deflection angles (δ_{lef}, δ_{tef}, and δ_{ht}) are downward.

The corresponding flow conditions for the selected configurations are then identified from the experimental data analyses at $M_\infty = 0.95$. Zero sideslip analyses are performed for all three configurations at $\alpha = 0°, 4°$, and 8° while the finite sideslip matrix composed of an α-sweep $(0°, 4°, 8°, 11°)$ at $\beta = 3°$ and a β-sweep $(0°, 3°, 6°)$ at $\alpha = 4°$. The selected computational matrix is depicted graphically in a chart form (figure 1) to illustrate the links between various configurations and the corresponding flow conditions. It should be noted that the transonic experimental data with finite sideslip angles were only available for the supersonic cruise configuration when the present computational analysis was initiated. In addition, the experiment was conducted to only measure the overall forces and moments.

COMPUTATIONAL GRID

The HSR Reference H initial surface geometry was defined in a format known as Initial Graphics Exchange Specification (IGES), (Ref. 2), which served as the database for all the subsequent grid generation processes. The GRIDTOOL (Ref. 3) program was used to read in the initial IGES geometry definition and the corresponding discretization into surface patches. The resulting surface patches were then read in the VGRID (Ref. 4) program to generate the initial surface triangulation by the advancing front method. The initial surface triangles were then read back into GRIDTOOL for the projection onto the initial database to preserve the proper surface curvature within the interior of a given patch. As a final step, the resulting front on the surface and the farfield boundary patches were used by VGRID to generate the volume grid within the computational domain along with the corresponding grid and face connectivity files. A nearfield and a closeup view of a typical grid, used to compute the flow for the transonic cruise configuration with deflected horizontal tail (i.e., $\delta_{lef} = 0/10$; $\delta_{tef} = 0/3$; $\delta_{ht} = 6$), are shown in figures 2 and 3 from two different perspectives. The figures illustrate the triangular meshes on the surface, plane of symmetry, and the wind-tunnel sting representation. The farfield boundaries, clipped in the figures for clarity, are extended to about 6-longitudinal and 3-radial body lengths away from the surface. The computational grid size for each of the three configurations are as follows: the transonic cruise configuration had about 1.023 million cells and 36,000 surface triangles; the transonic cruise with deflected horizontal tail configuration had 0.822

million cells and 44,000 surface triangles; and the supersonic cruise configuration had 0.997 million cells and 47,000 surface triangles. The grid for the supersonic cruise configuration was mirrored about the symmetry plane to generate the computational grid for all the finite sideslip runs. The resulting grid approximately doubled the grid size used for the zero sideslip (only one-half modeled) computations.

ALGORITHM PERFORMANCE AND CONVERGENCE

USM3D computations were performed on both the Numerical Aerodynamic Simulation (NAS) Cray-C90 located at NASA Ames, and the NASA Langley Cray-YMP. All the zero sideslip computations were conducted on the Cray-C90 using the implicit time integration scheme and the corresponding finite sideslip cases were executed on the Cray-YMP by using the explicit algorithm. Also, no flux limiters were used to obtain the solutions presented here. As a general strategy, solutions based on the second-order accurate flux difference splitting (FDS2) method were first sought; however, for certain cases only the first-order accurate flux difference splitting (FDS1) could be achieved. In general, the aerodynamic effects due to the difference in the order of solution accuracy were found to be small, particularly in terms of total forces and moments and will be discussed later.

The selected computational matrix, along with the corresponding numerical method employed to converge a given solution for each configuration, are summarized in Table 1. In this table, symbols '$\surd$' and 'X' indicate that a solution convergence 'was' and 'was not' achieved, respectively. For zero sideslip cases, converged solutions with FDS2 were obtained for all configurations at $\alpha = 0°$ and 4°, except for the supersonic cruise configuration at $\alpha = 4°$ where only the FDS1 solution could be achieved. At higher angles of attack (i.e., $\alpha > 4°$), no solution convergence based on FDS2 could be achieved for any of the configurations investigated. It is speculated that the lack of solution convergence could be due to the flow separation occurring within the boundary layer over the round leading-edges of the inboard wing which is known to require Navier-Stokes simulation to resolve. As a result, the numerical solutions for $\alpha = 8°$ are obtained based on FDS1 for all the configurations except for the supersonic cruise configuration for which no solution could be achieved. The supersonic cruise configuration was the most challenging geometry to obtain solution convergence at the present transonic flow conditions. The solution convergence difficulties were identified to have been caused primarily by geometrical features particularly with respect to the transition region between the inboard and the outboard wing. This transition region represents a step discontinuity from a round to a sharp leading edge of the undeflected flap on the outboard wing. Progress has been made recently to implement various flux limiters in USM3D as numerical dumping mechanisms to alleviate such convergence difficulties. As mentioned earlier, the supersonic cruise configuration was the only geometry for which experimental data were available at transonic speeds with finite sideslip angle. As a result, with the lessons learned from the zero sideslip computations, only FDS1 solutions were sought for the finite sideslip analysis. A typical zero sideslip case required about 500 cycles to converge and, for finite sideslip cases, required about 1000 cycles. The implicit time integration scheme required $\approx$ 180 words of memory per cell and $\approx$ 30 μ-second/cell/cycle on the Cray-C90. Similarly, the explicit scheme required $\approx$ 46 words of memory per cell and $\approx$ 6 μ-second/cell/cycle on the Cray-C90. Very little overhead CPU time, generally less than 5%, is found to be associated with the second-order accurate solution, compared to the first-order formulation.

Typical convergence characteristics (i.e., Residuals and Lift) for solutions based on FDS2 and FDS1 at $\alpha = 0°$, $\beta = 0°$, for the supersonic cruise configuration are shown in Figures 4(a) and 4(b), respectively. A typical second-order solution is initiated automatically within USM3D after a certain level of residual convergence has been achieved by the first-order accurate flux formulation. For example, as shown in figure 4(a), the FDS2 solution is initiated from the FDS1 solution (after 205 iterations) where the residuals have already dropped 2.5 orders of magnitude. Similarly, figure 4(b) shows the residual and lift characteristics for the fully converged solution based on the FDS1 formulation. These two particular solutions were obtained as part of the solution accuracy assessment between first- and second- order flux differencing schemes. A similar set of convergence history plots are shown in figure 5 for typical solutions obtained for the supersonic cruise configuration for two different sideslip angles at $\alpha = 4°$.

RESULTS AND DISCUSSIONS

Surface Pressure Coefficients:

Typical surface pressure coefficient contours computed at $\alpha = 4°$, $M_\infty = 0.95$, and $\beta = 0°$ for the transonic cruise, transonic cruise with deflected horizontal tail, and the supersonic cruise configurations, are shown in figures 6, 7 and 8, respectively. All surface pressure coefficients are contoured over a constant range from 0.6 to -1.4 with 0.067 increments (i.e., $C_{pmax} = 0.6$, $C_{pmin} = -1.4$, $\Delta C_p = 0.067$) and shown from the same vantage point. The surface pressure contours computed for the transonic cruise configuration, shown in figure 6, serve as the baseline solution to be correlated with the results obtained for the transonic cruise configuration with deflected horizontal tail and the supersonic cruise configuration. The latter two correlations show the effects of horizontal tail deflection and the wing leading-edge and trailing-edge flap deflections on the computed surface pressure coefficients, respectively. Furthermore, since no experimental surface pressure data is available, these correlations are only intended for relative comparisons between computational results to show, qualitatively, the effects due to a particular control surface deflection.

The surface pressure coefficients computed for the baseline transonic cruise configuration (figure 6) can be characterized by two dominant flow features, one that can be attributed to typical flow expansions caused by the physical geometry and the other to shock waves due to the transonic flow effects. The typical flow expansions on the upper surface (figure 6(a)) occur at the leading edges, particularly on the inboard wing, and the hinge lines associated with the deflected leading-edge and trailing-edge flaps on the outboard wing. The transonic flow shock waves (i.e., highlighted by a concentration of several pressure contour lines) on the upper surface appear in two locations. The first location is very close, nearly spanning in parallel, to the entire wing trailing edge, and the other location is situated approximately along the mid-chord, spanning the horizontal tail and extending to the fuselage and onto the vertical tail. The lower surface pressure contours (figure 6(b)) indicate fairly benign flow characteristics with the exception of a shock wave that appears in between the two nacelles and the compression rings on the wing just ahead of each nacelle caused by the pylons.

The comparative assessments of the results shown in figures 6 and 7 indicate only very small effects due to the horizontal tail deflection on the computed surface pressure coefficient contours for the transonic cruise configuration. The most noticeable change appears to be the flip of the shock wave from the upper surface of the undeflected horizontal tail to the lower surface of the deflected horizontal tail. Similarly, a comparison of the results shown in figures 6 and 8 indicate the effects of wing leading-edge and trailing-edge flap deflections on the computed surface pressure coefficient contours for the transonic cruise configuration. As expected, the comparison indicates that the hinge line flow expansions disappear on the upper surface of the undeflected wing leading-edge and trailing-edge flaps. In addition, the shock waves on the wing upper surface near the wing trailing edge and the horizontal tail, for the supersonic cruise configuration, are not as crisply predicted as those of the transonic cruise configuration. This smearing of the shock waves is speculated to have been caused primarily by the excess dissipation generally associated with the first-order accurate solutions. The comparison shows very little difference on the computed lower surface pressure coefficient contours due to wing leading-edge and trailing-edge flap deflections.

Forces and Moments and Correlations with Data:

All predicted inviscid drag coefficients have been corrected with an appropriate C_{Do} to account for the skin friction using the experimental data obtained in the NASA LaRC 16-Foot Transonic Tunnel. This C_{Do} was determined by a linear extrapolation from the plotted C_L^2 vs. C_D curve for the supersonic cruise configuration as shown in figure 9. This C_{Do} provides a minimum skin friction drag which, by definition, is independent of the configuration camber and twist. Through this analysis, a C_{Do} of 0.0126 was obtained, which was subsequently added to all the inviscid drag predictions.

Solution method assessment - As discussed earlier, the supersonic cruise configuration was the most challenging geometry for obtaining solution convergence at the present transonic Mach number. As a result,

the FDS2 solution could only be achieved for $\alpha = 0°$, and the FDS1 solution could only be achieved for $\alpha = 4°$. This prompted a solution method assessment study to be performed at $\alpha = 0°$ for which both first- and second- order solutions could be obtained. The results from this study are presented in figure 10 for the longitudinal aerodynamic characteristics. The correlations at $\alpha = 0°$ indicate that the solution order of accuracy has only a small effect on the predicted lift and drag, with relatively more pronounced effect on the pitching moment estimate.

Horizontal tail deflection effects - The predicted and measured longitudinal aerodynamic effects due to the horizontal tail deflection at $M_\infty = 0.95$ and $\beta = 0°$ are shown in figure 11. The measured aerodynamic effects due to the horizontal tail deflection on both the lift and drag coefficients appear to be small. The pitching moment characteristics remain nearly the same over the measured range of flow conditions, and as expected, the horizontal tail deflection causes roughly a constant positive shift in the pitching moment coefficients. The overall lift and drag coefficients have been predicted reasonably well with the Euler method both in terms of incremental effects due to the horizontal tail deflection and magnitudes. Although the overall magnitudes of the pitching moment coefficients are not predicted as well, the incremental effects due to the horizontal tail deflection are predicted reasonably well.

Wing leading-edge and trailing-edge flap deflection effects - The predicted and measured longitudinal aerodynamic effects due to the leading-edge and trailing-edge flap deflection at $M_\infty = 0.95$ and $\beta = 0°$ are shown in figure 12. The measured aerodynamic effects due to the leading-edge and trailing-edge flap deflections appear to be small for both the lift and drag coefficients and more pronounced for the pitching moment characteristics particularly at $\alpha \leq 10°$. These aerodynamic effects due to the leading-edge and trailing-edge flap are reasonably predicted both in terms of overall magnitudes and trends.

Finite sideslip stability analysis - The longitudinal aerodynamic characteristics computed for an α-sweep (i.e., $0°, 4°, 8°$, and $11°$) at $\beta = 3°$ and $M_\infty = 0.95$, along with the experimental measurements for the supersonic cruise configuration, are shown in figure 13. The correlations indicate excellent agreement between the computed and measured data throughout the examined range of flow conditions for both magnitudes and trends.

The lateral/directional stability characteristics computed for a β-sweep (i.e., $0°, 3°$, and $6°$) at $\alpha = 4°$ and $M_\infty = 0.95$, along with the experimental measurements for the supersonic cruise configuration, are shown in figure 14. The correlations indicate a good agreement for the pitching and rolling moments but not as good for the yawing moment, particularly with respect to the slope (i.e., $C_{n\beta}$).

CONCLUDING REMARKS

The application viability of an unstructured grid Euler method (USM3D) for predicting the longitudinal and lateral/directional stability characteristics of the HSR Reference H configuration at a transonic Mach number of 0.95 have been addressed. Particular emphasis was placed on assessing the ability of the method to provide consistent and accurate solutions of forces and moments for the baseline configuration with different control surface deflection settings for the horizontal tail as well as for the leading-edge and trailing-edge flaps. The analysis revealed that a consistent set of solutions based on the first-order accuracy was achievable for a wider range of applicability (in terms of configurations and flow conditions) where the second-order accurate solutions could not be obtained. The solution method assessment analysis indicated that the first-order accurate solutions provide comparable results to those of the second-order, particularly for the aggregate forces and moment characteristics. The computed longitudinal aerodynamic effects due to control surface deflections and sideslip angles agree reasonably well with the measured data both in terms of magnitude and trends. Finally, the lateral/directional stability analysis revealed fairly good agreement between the predictions and measured data for the pitching and rolling moment characteristics but not as good for the yawing moment. It is believed that the present unstructured grid Euler method is certainly a viable engineering tool that can be utilized with confidence in the early aerodynamic design and analysis of the proposed high speed civil transport configuration.

REFERENCES

[1] Frink, N. T., "Upwind Scheme for Solving the Euler Equations on Unstructured Tetrahedral Meshes," AIAA Journal, Vol. 30, No. 1, 1992, pp. 70-77.

[2] Smith, B. M.; Brauner, K. M.; Kennicott, P. R.; Liewald, M.; and Wellington, J.: Initial Graphics Exchange Specification (IGES), Version 2.0. NBSIR-82-2631-AF, Feb. 1983. (Available from NTIS as PB 83-137448.)

[3] Abolhassani, J. "GRIDTOOL: A Surface Modeling and Grid Generation Tool," NASA-CP-3291, May 1995, pp. 821-832.

[4] Parikh, P., Pirzadeh, S., and Lohner, R., "A Package for 3-D Unstructured Grid Generation, Finite-Element Flow Solution and Flow Field Visualization," NASA CR-182090, Sept. 1990.

	FDS2			FDS1		
Configuration \ α	0°	4°	8°	0°	4°	8°
Transonic cruise	√	√	X	--	--	√
Transonic cruise with $\delta_{ht} = 6$	√	√	X	--	--	√
Supersonic cruise	√	X	X	√	√	X

Table 1.- Computational matrix - method of convergence.

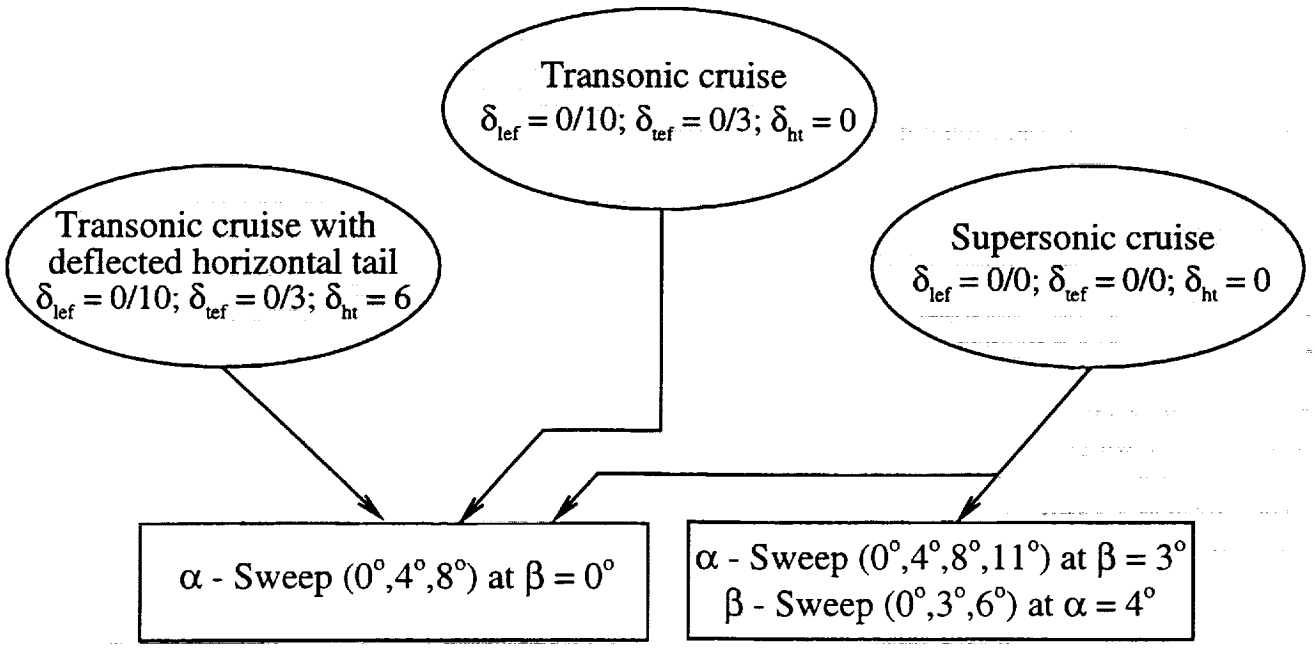

Figure 1.- Selected computational matrix - geometries and conditions.

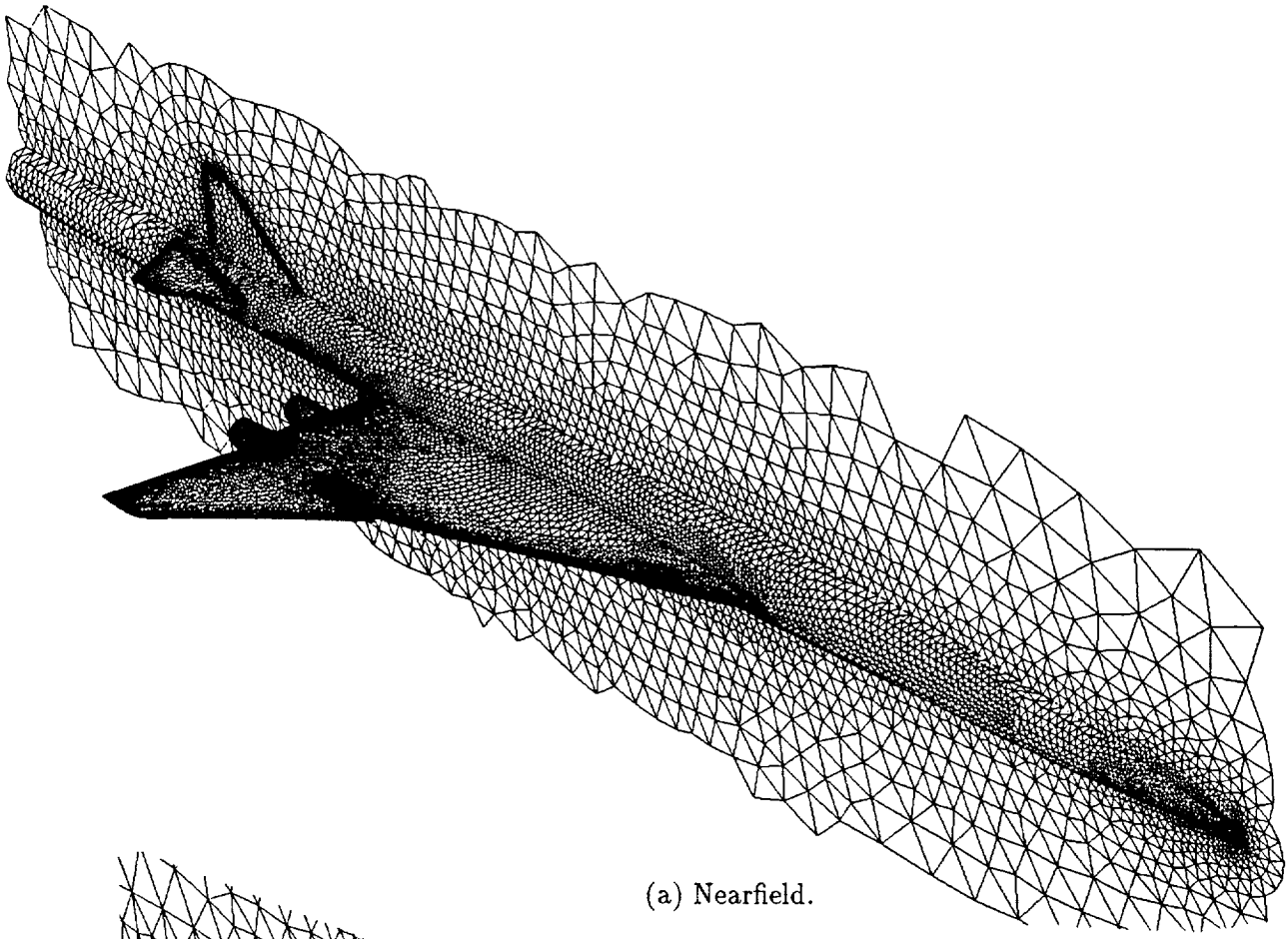

(a) Nearfield.

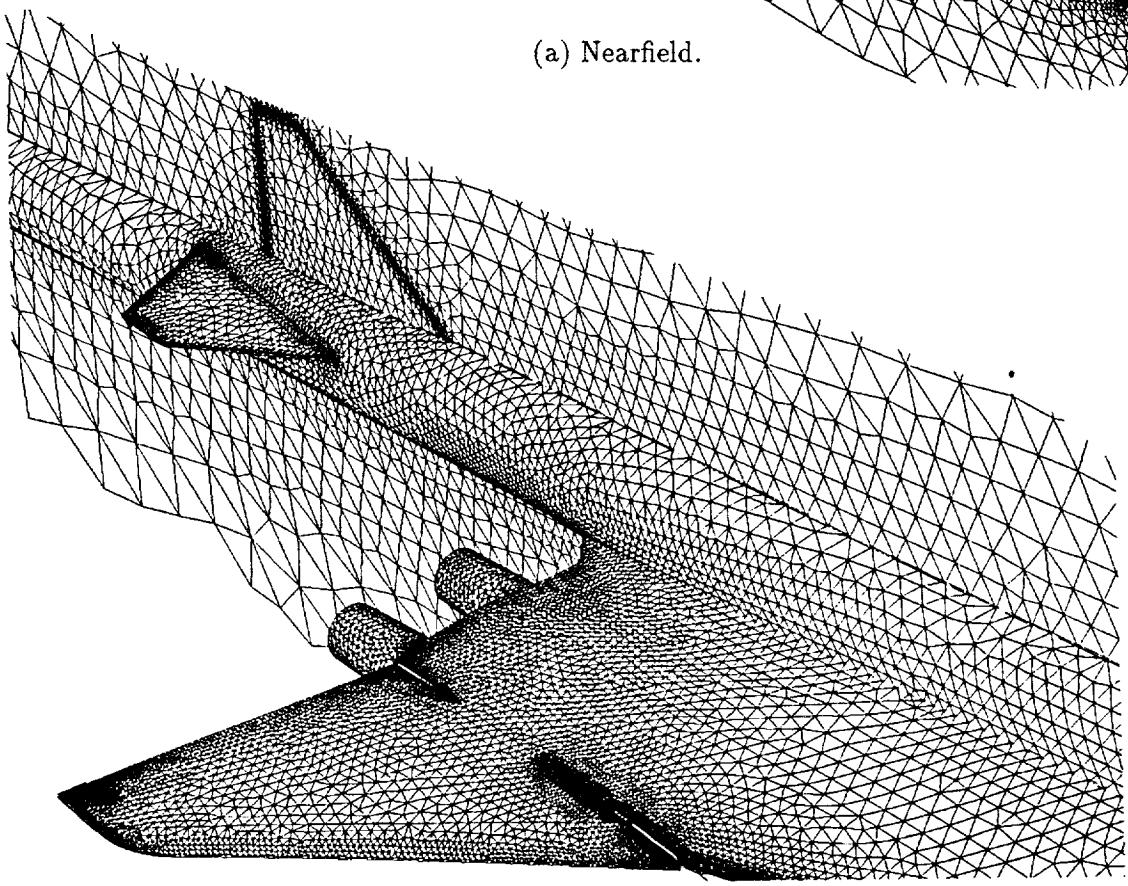

(b) Closeup.

Figure 2.- Typical computational grid - Upper surface view. $\delta_{lef} = 0/10$, $\delta_{tef} = 0/3$, $\delta_{ht} = 6$.

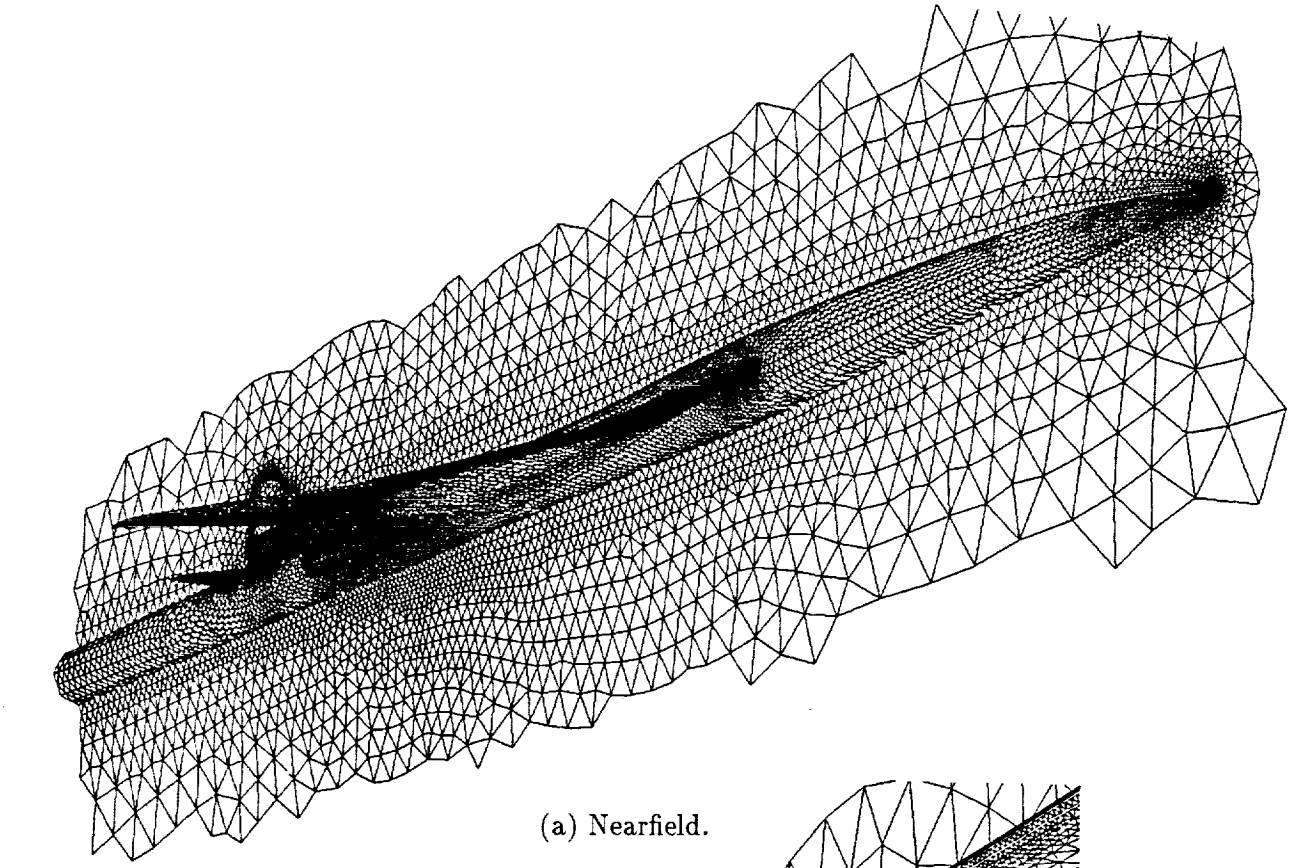

(a) Nearfield.

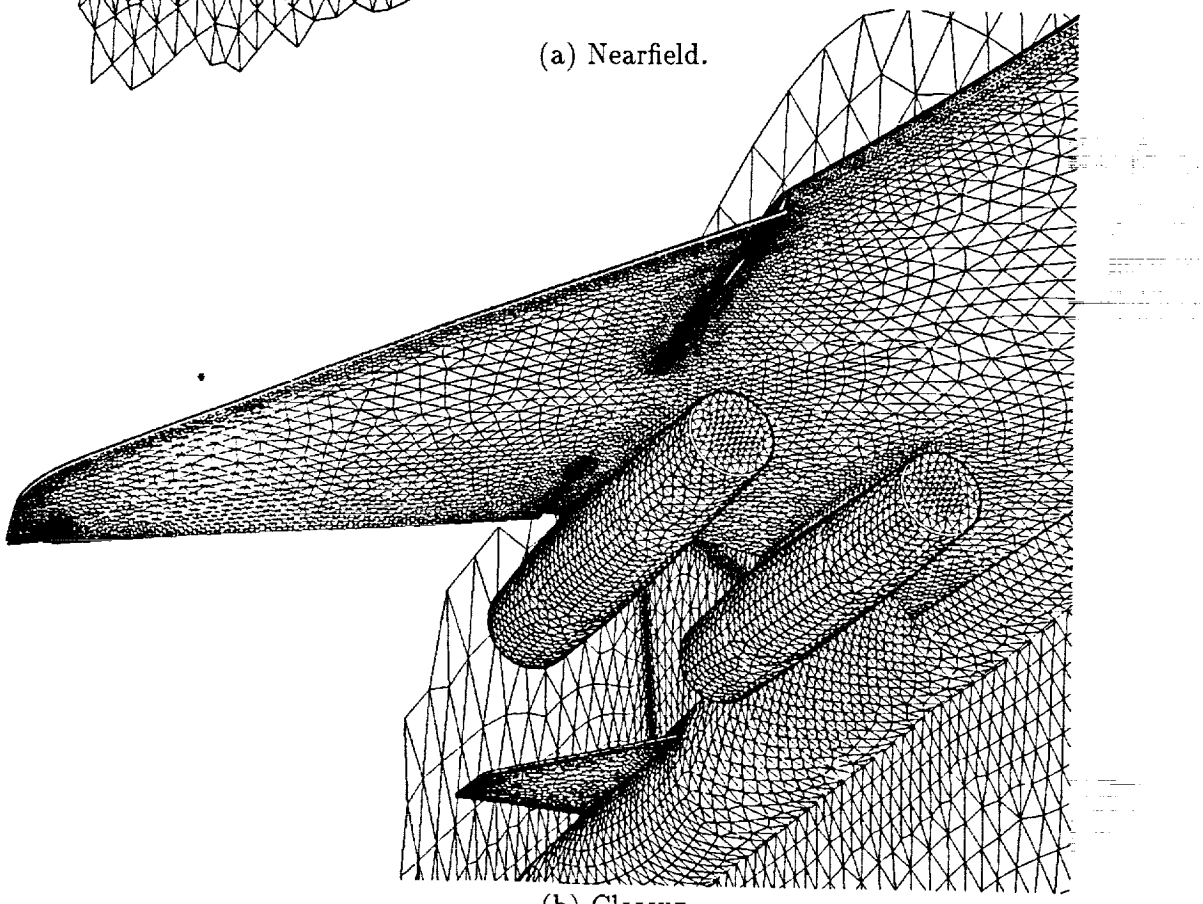

(b) Closeup.

Figure 3.- Typical computational grid - Lower surface view. $\delta_{lef} = 0/10$, $\delta_{tef} = 0/3$, $\delta_{ht} = 6$.

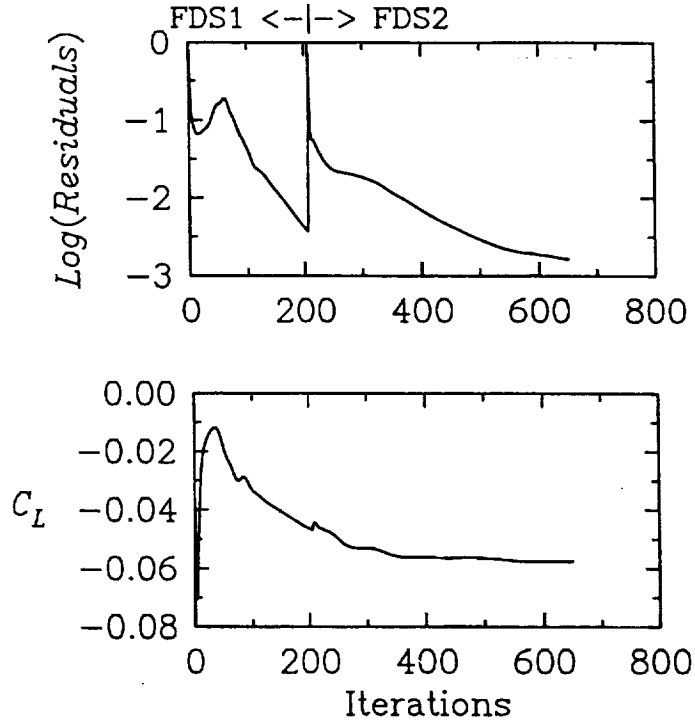

(a) FDS2.

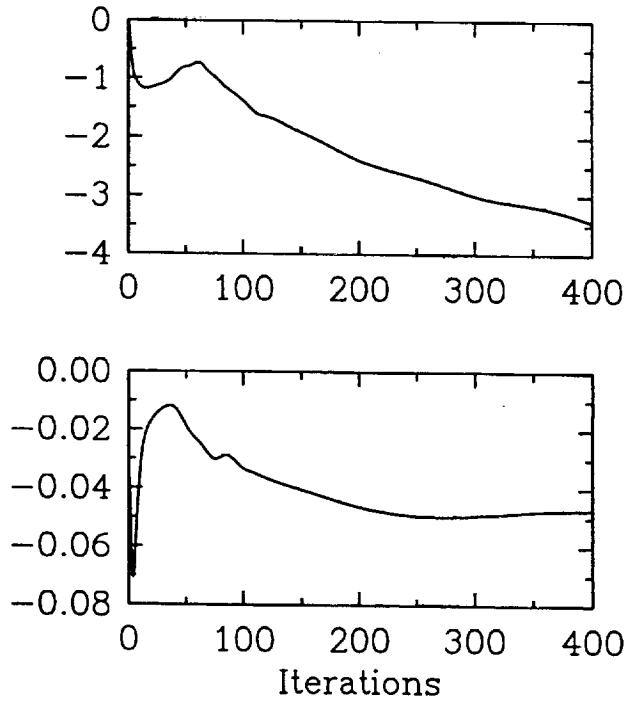

(b) FDS1.

Figure 4.- Typical convergence characteristics - $\delta_{lef} = 0/0$, $\delta_{tef} = 0/0$, $\delta_{ht} = 0$; $M_\infty = 0.95$, $\alpha = 0°$, $\beta = 0°$.

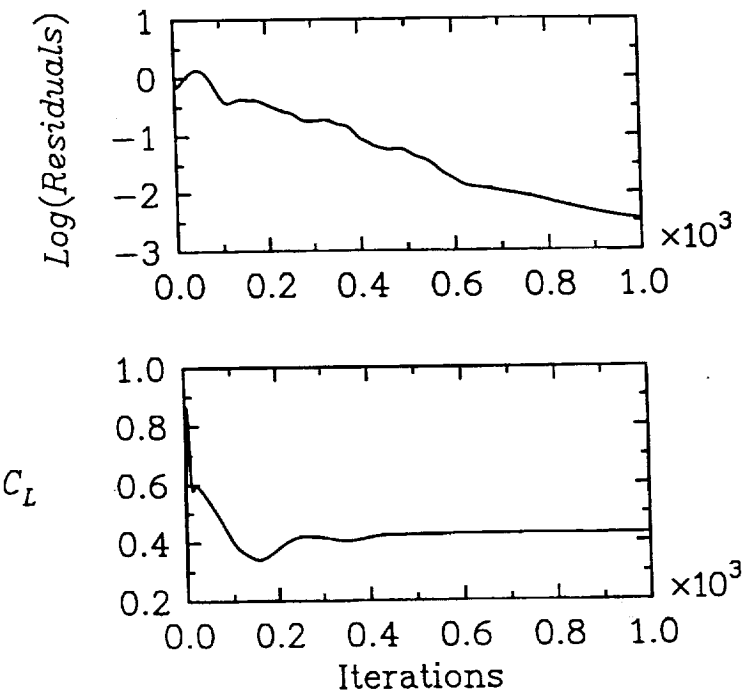

(a) $\beta = 3°$.

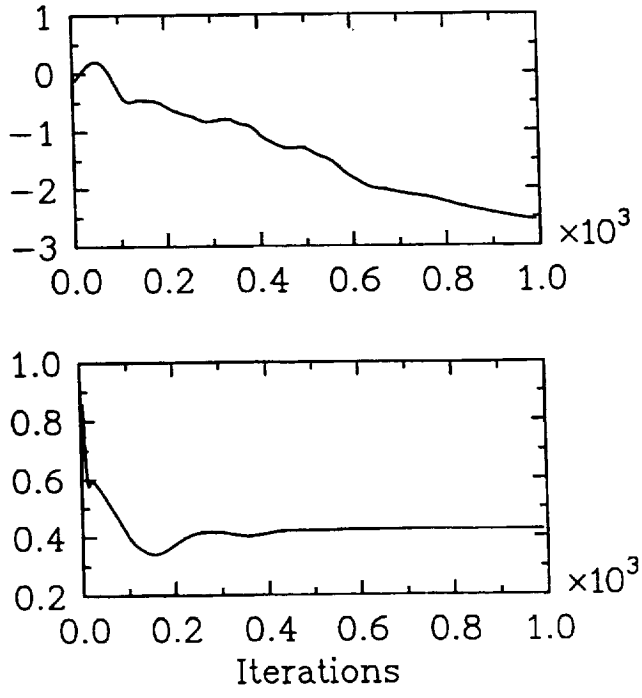

(b) $\beta = 6°$.

Figure 5.- Typical FDS1 convergence characteristics - $\delta_{lef} = 0/0$, $\delta_{tef} = 0/0$, $\delta_{ht} = 0$; $M_\infty = 0.95$, $\alpha = 0°$.

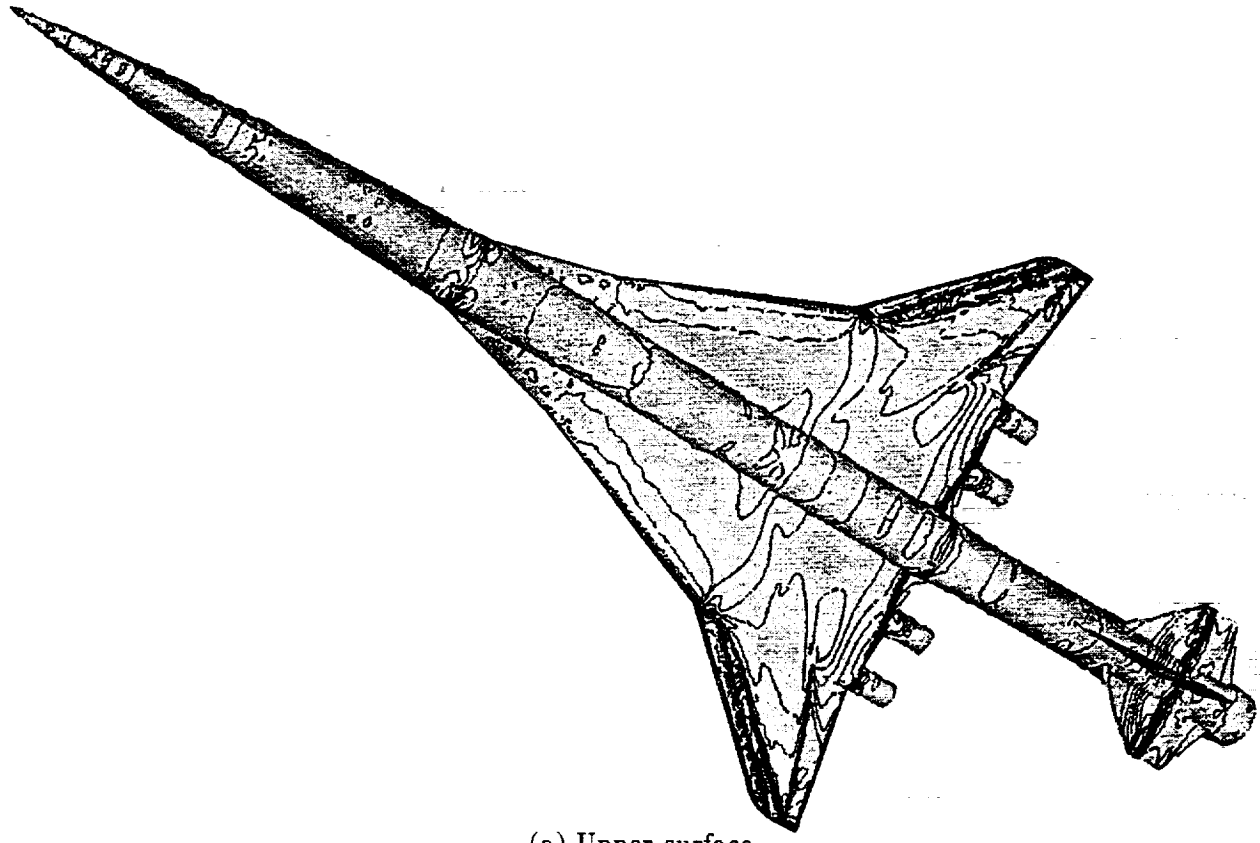

(a) Upper surface.

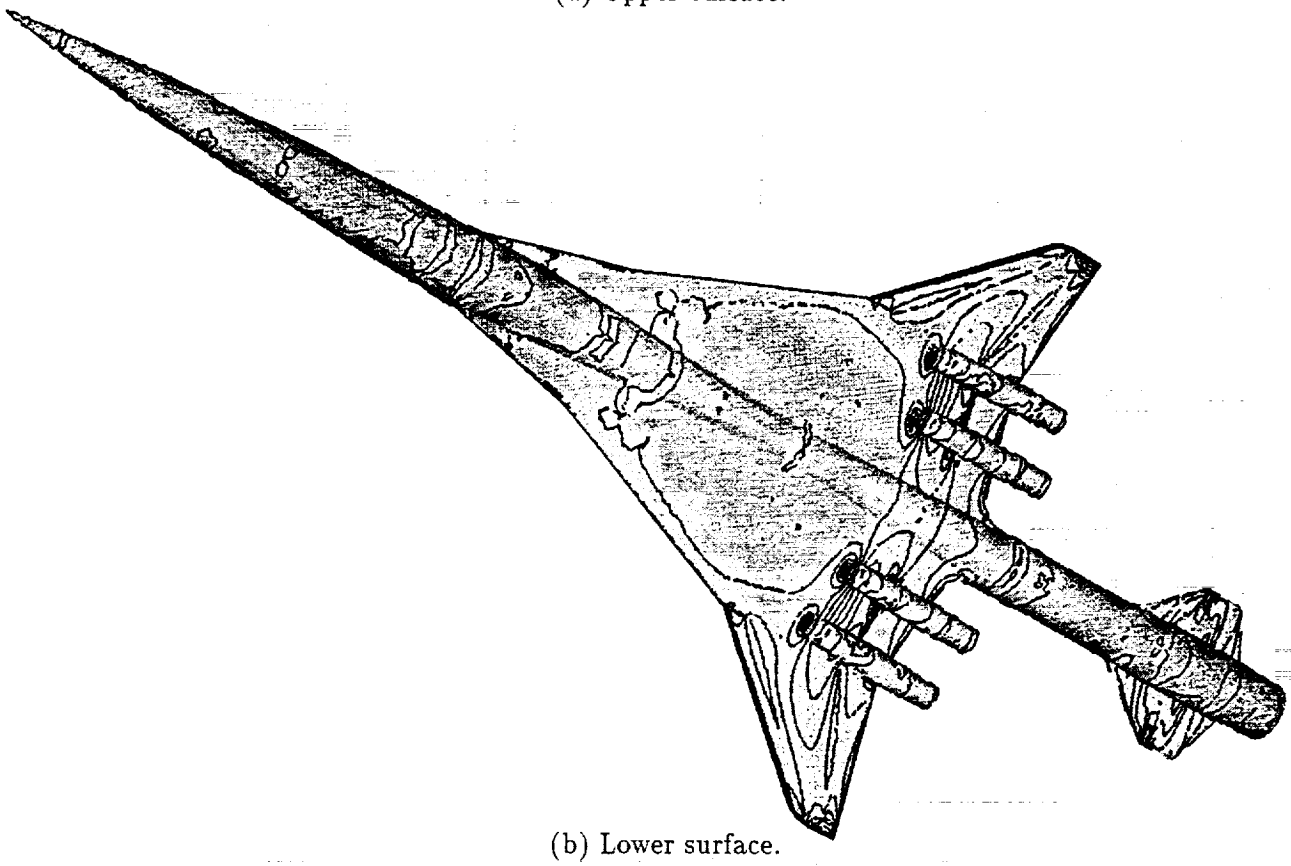

(b) Lower surface.

Figure 6.- Computed surface C_p contours - Transonic cruise geometry. $M_\infty = 0.95$, $\alpha = 4°$, $\beta = 0°$.

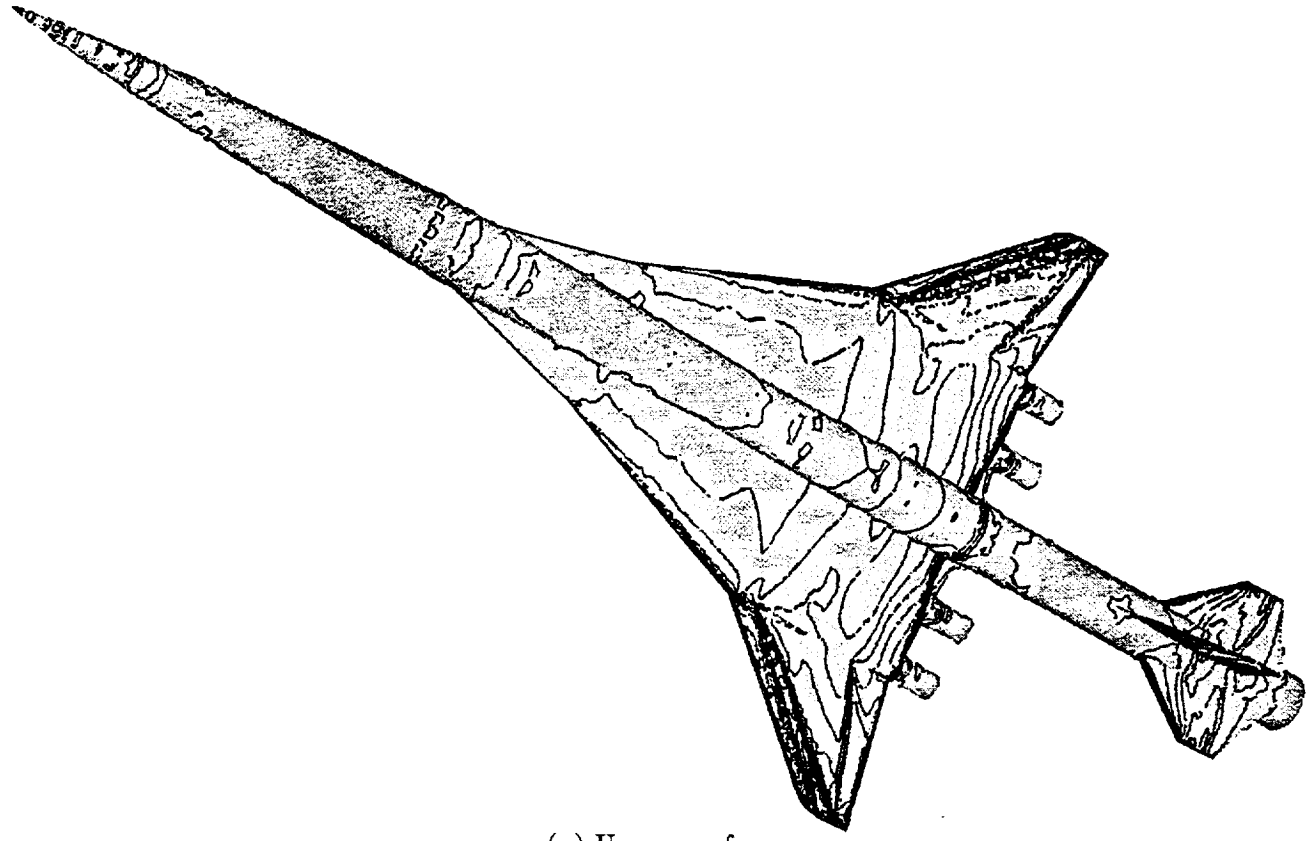

(a) Upper surface.

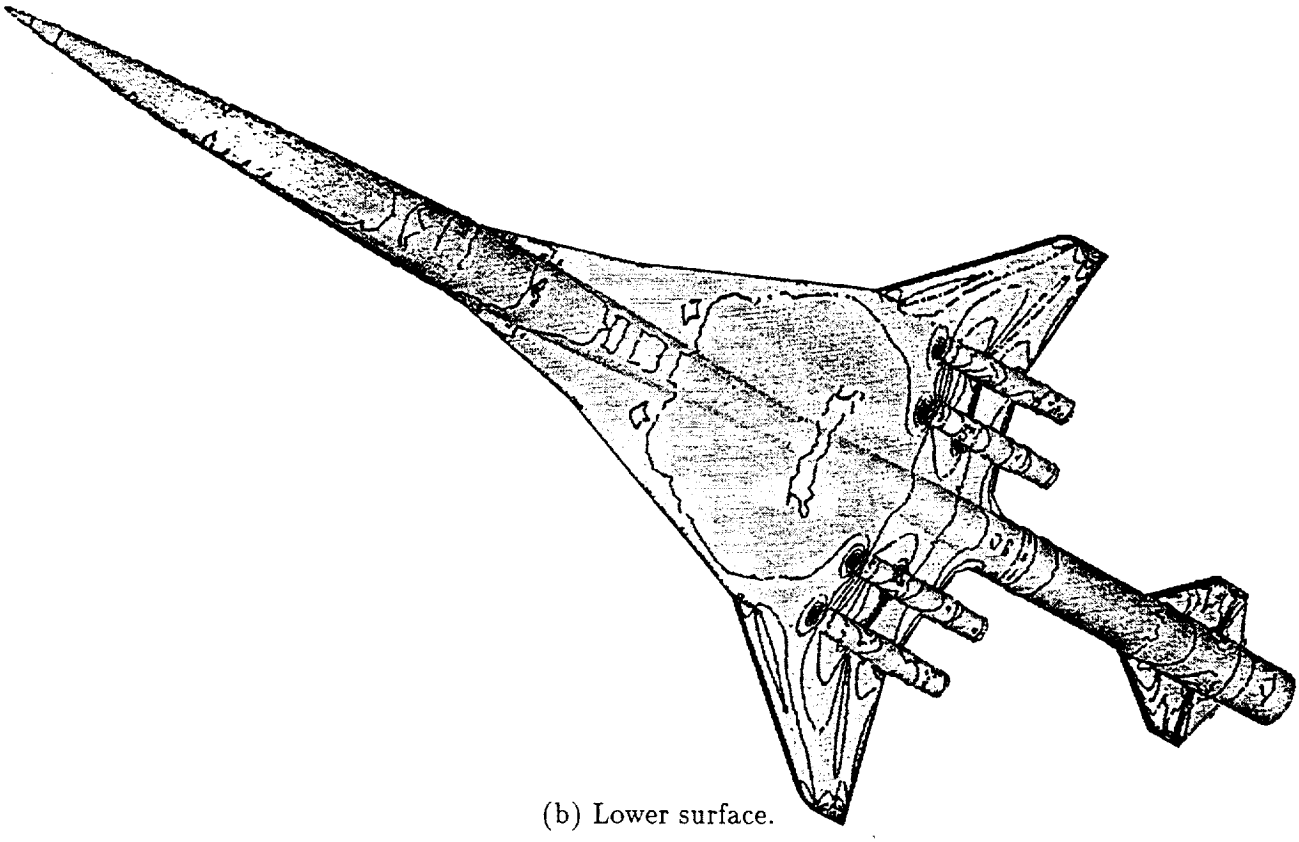

(b) Lower surface.

Figure 7.- Computed surface C_p contours - Transonic cruise geometry with $\delta_{ht} = 6.$. $M_\infty = 0.95$, $\alpha = 4°$, $\beta = 0°$.

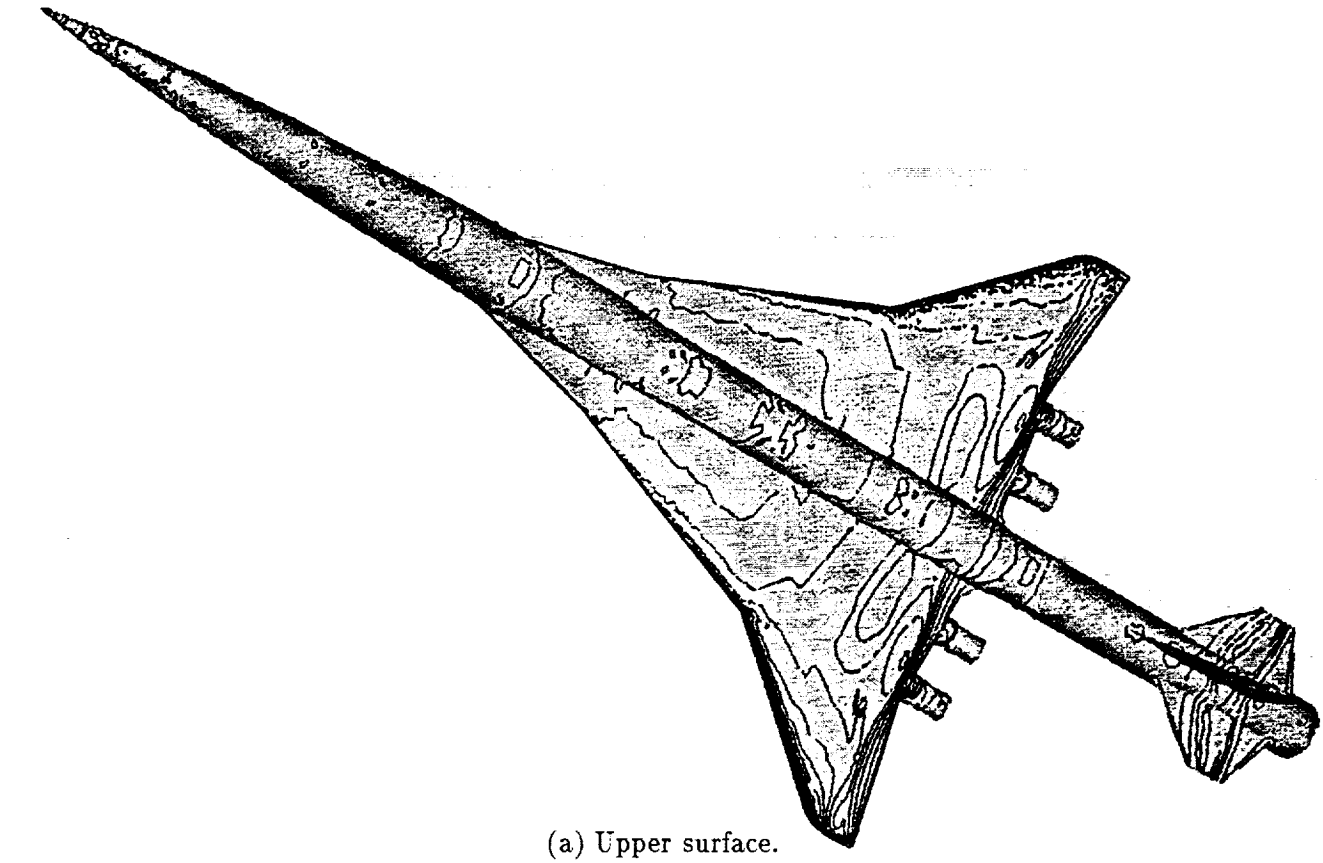

(a) Upper surface.

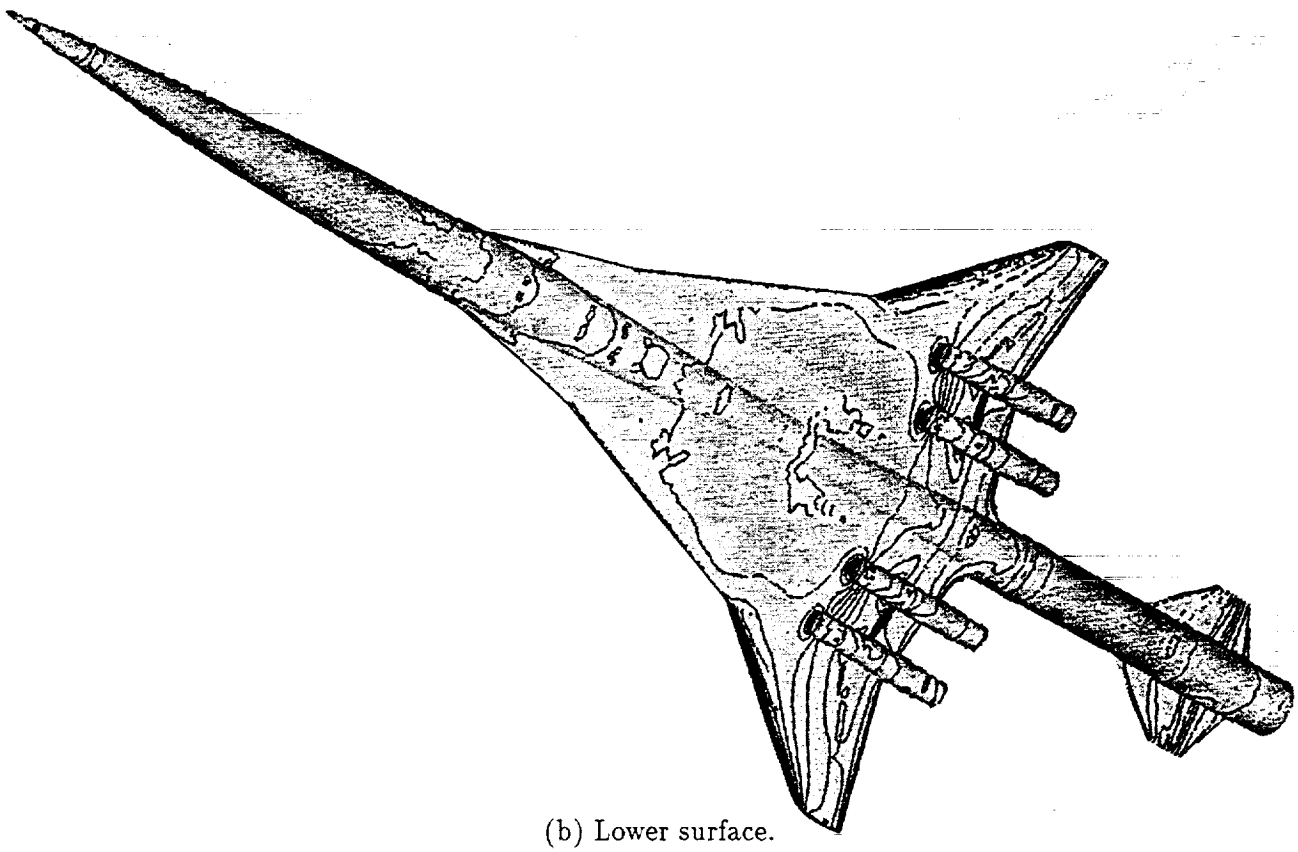

(b) Lower surface.

Figure 8.- Computed surface C_p contours - Supersonic cruise geometry. $M_\infty = 0.95$, $\alpha = 4°$, $\beta = 0°$.

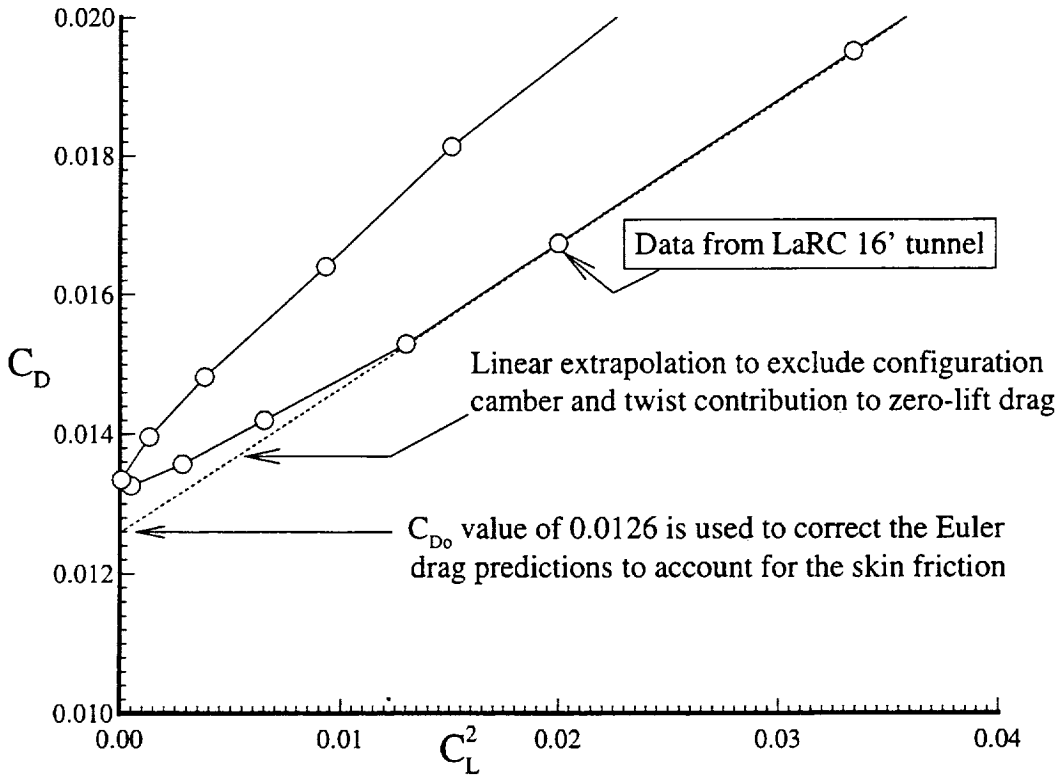

Figure 9.- C_{Do} determination strategy - Supersonic cruise geometry, $M_\infty = 0.95$

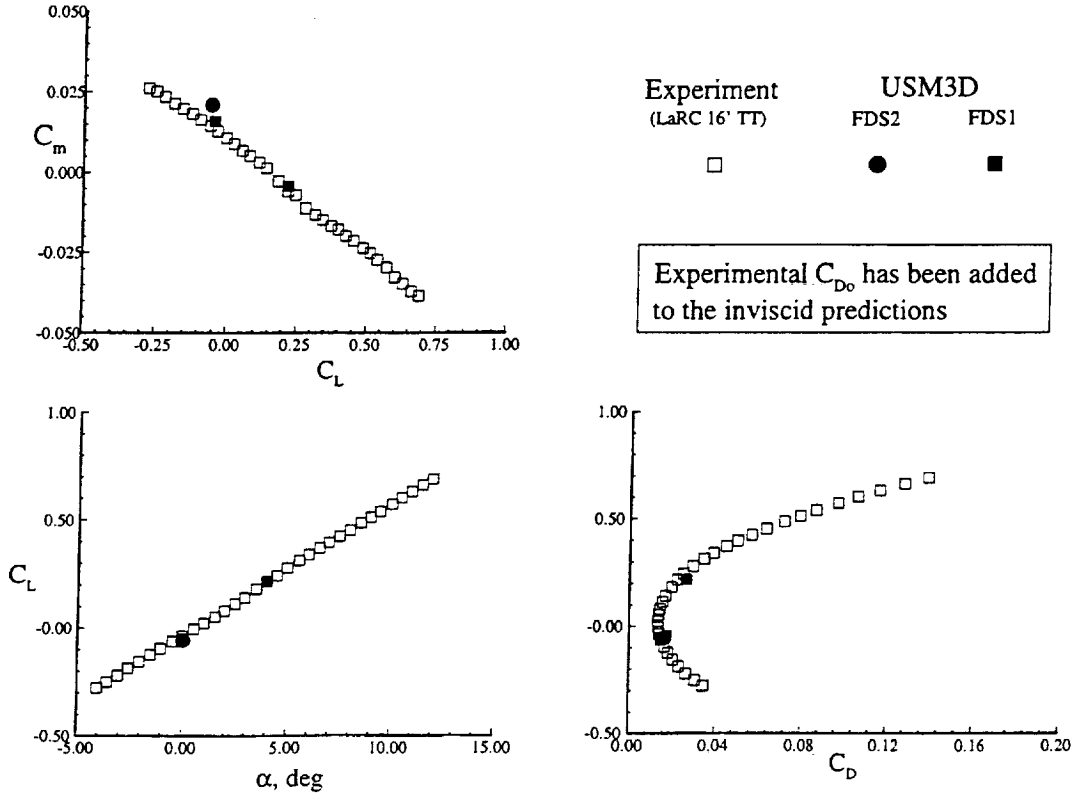

Figure 10.- Solution method accuracy assessment - Supersonic cruise geometry, $M_\infty = 0.95$, $\beta = 0°$.

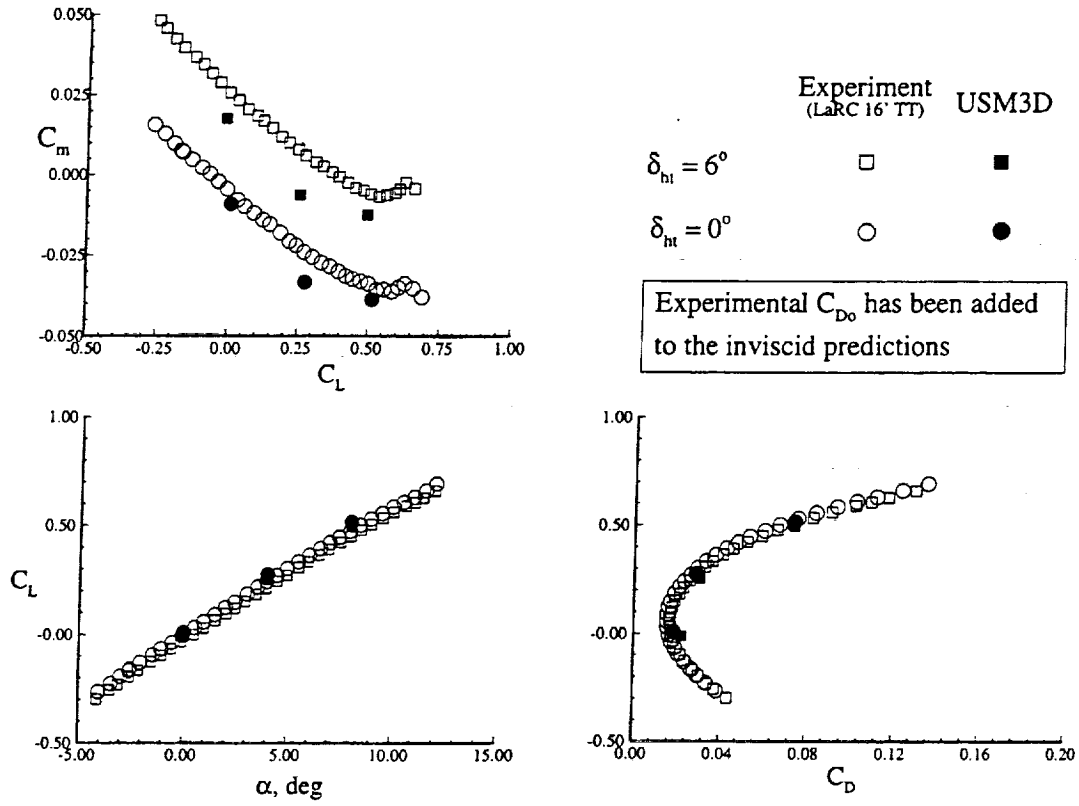

Figure 11.- Horizontal tail deflection effects and predictions - Transonic cruise geometry, $M_\infty = 0.95$, $\beta = 0°$.

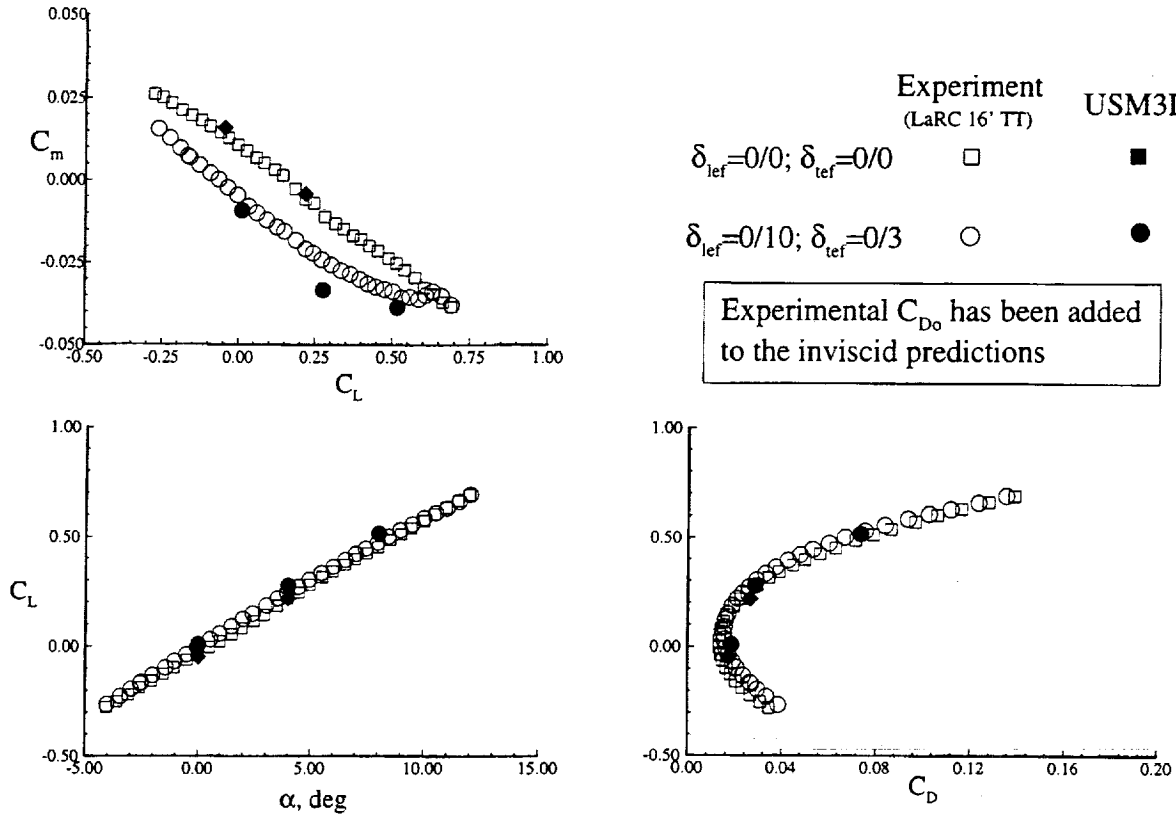

Figure 12.- Leading/trailing-edge flap deflection effects and predictions - Transonic cruise geometry, $M_\infty = 0.95$, $\beta =$

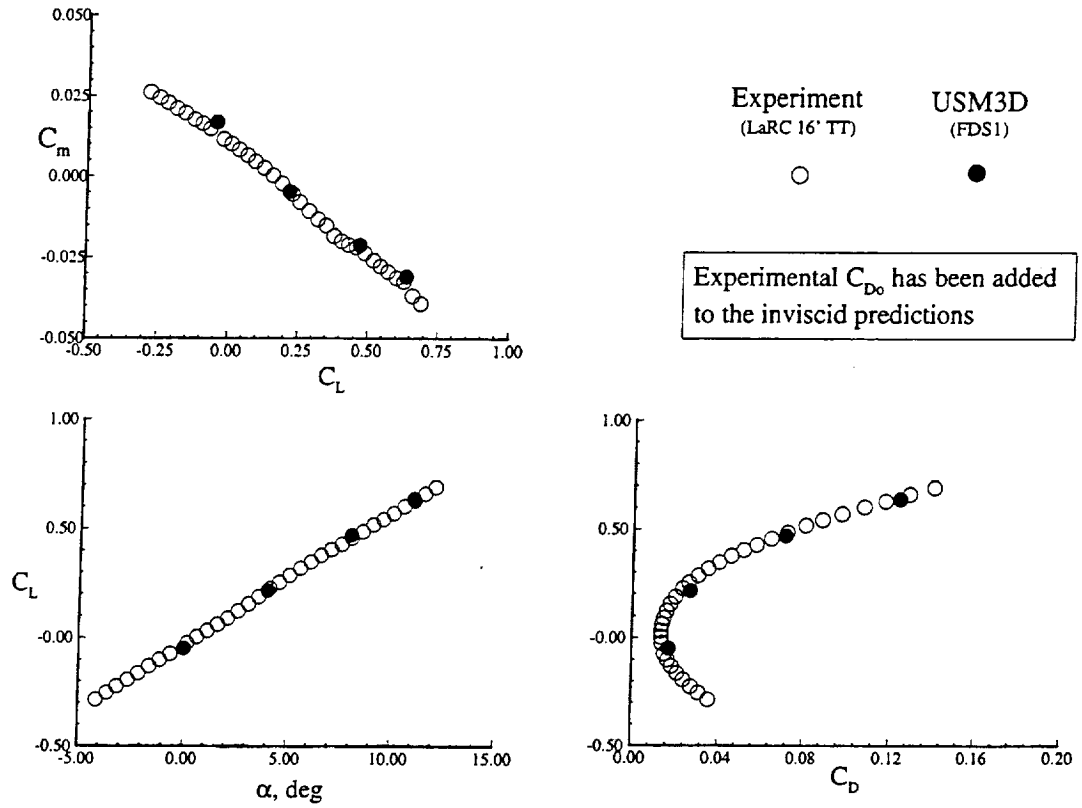

Figure 13.- Longitudinal aerodynamic characteristics and predictions - Supersonic cruise geometry, $M_\infty = 0.95$, $\beta = 3°$.

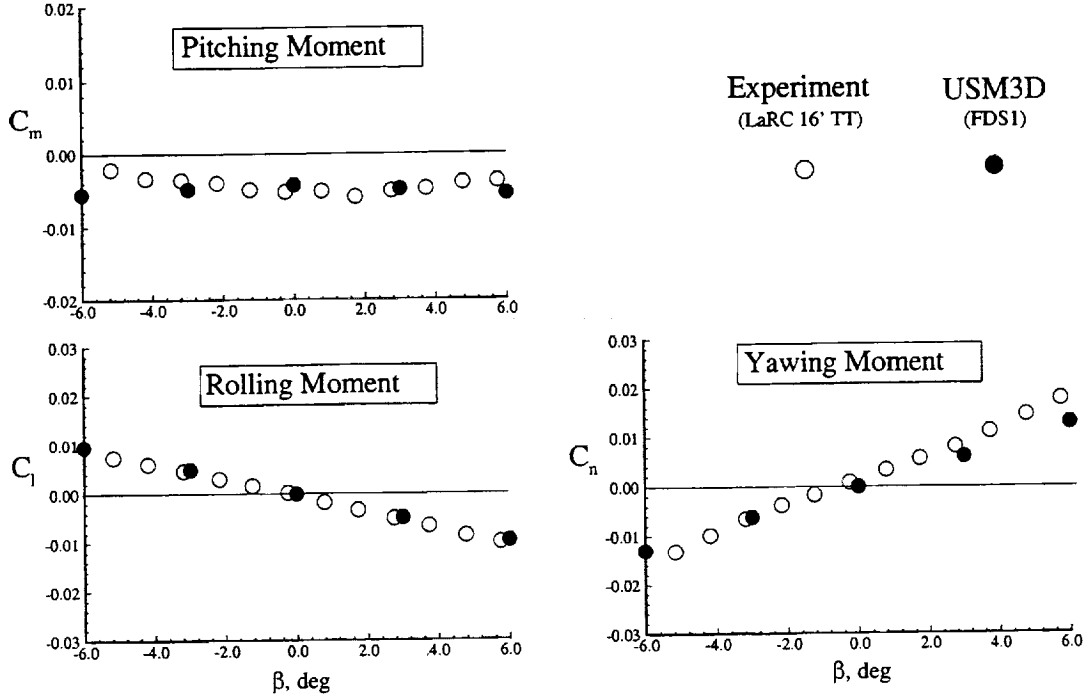

igure 14.- Lateral/directional stability characteristics and predictions - Supersonic cruise geometry, $M_\infty = 0.95$, $\alpha = 4°$.

REPORT DOCUMENTATION PAGE

Form Approved
OMB No. 0704-0188

1. AGENCY USE ONLY *(Leave blank)*	2. REPORT DATE	3. REPORT TYPE AND DATES COVERED
	December 1999	Technical Memorandum

4. TITLE AND SUBTITLE
Unstructured Grid Euler Method Assessment for Longitudinal and Lateral/Directional Stability Analysis of the HSR Reference H Configuration at Transonic Speeds

5. FUNDING NUMBERS
WU 537-07-20-21
WBS 4.3.1

6. AUTHOR(S)
Farhad Ghaffari

7. PERFORMING ORGANIZATION NAME(S) AND ADDRESS(ES)
NASA Langley Research Center
Hampton, VA 23681-2199

8. PERFORMING ORGANIZATION REPORT NUMBER
L-17927

9. SPONSORING/MONITORING AGENCY NAME(S) AND ADDRESS(ES)
National Aeronautics and Space Administration
Washington, DC 20546-0001

10. SPONSORING/MONITORING AGENCY REPORT NUMBER
NASA/TM-1999-209526

11. SUPPLEMENTARY NOTES

12a. DISTRIBUTION/AVAILABILITY STATEMENT
Unclassified–Unlimited
Subject Category 02 Distribution: Nonstandard
Availability: NASA CASI (301) 621-0390

12b. DISTRIBUTION CODE

13. ABSTRACT ***(Maximum 200 words)***
Transonic Euler computations, based on unstructured grid methodology, are performed for a proposed High Speed Civil Transport (HSCT) configuration, designated as the Reference H configuration within the High Speed Research (HSR) Program. The predicted results are correlated with appropriate experimental wind-tunnel data for the baseline configuration with and without control surface deflections for a range of angle of attack at $M_\infty = 0.95$. Good correlations between the predictions and measured data have been obtained for the longitudinal aerodynamic characteristics of the baseline configuration. The incremental effects in the longitudinal aerodynamic characteristics due to horizontal rail deflections as well as wing leading-edge and trailing-edge flap deflections have also been predicted reasonably well. Compuational results and correlations with data are also presented for the lateral and directional stability characteristics for a range of angle of attack at a constant sideslip angle as well as a range of sideslip angles at a constant angle of attack. In addition, the results are presented to assess the computational method performance and convergence characteristics.

14. SUBJECT TERMS	15. NUMBER OF PAGES
Computational fluid dynamics; Euler/inviscid method; High speed research/High Speed Civil Transport Reference H; Unstructured grid; Transonic speeds; Longitudinal and lateral/directional	20
	16. PRICE CODE A03

17. SECURITY CLASSIFICATION OF REPORT	18. SECURITY CLASSIFICATION OF THIS PAGE	19. SECURITY CLASSIFICATION OF ABSTRACT	20. LIMITATION OF ABSTRACT
Unclassified	Unclassified	Unclassified	UL